Available online at www.sciencedirect.com
ScienceDirect
Acta Materialia 59 (2011) 146–158
Acta MATERIALIA
www.elsevier.com/locate/actamat

Mechanical properties of directionally freeze-cast titanium foams

Jessica C. Li, David C. Dunand *

Department of Materials Science and Engineering, Northwestern University, Evanston, IL 60208, USA

Received 30 July 2010; received in revised form 10 September 2010; accepted 10 September 2010

Abstract

Titanium foams with aligned, elongated pores were created by directional freeze-casting of aqueous slurries of titanium powders, followed by ice sublimation and powder sintering. Increasing sintering times from 8 to 24 h and decreasing powder size from 20 to 10 μm resulted in improved densification within cell walls and decreased overall foam porosity, with a concomitant increase in compressive stiffness, yield strength and energy absorption. A simple model for foam stiffness and strength is in general agreement with experimental measurements of strength but overpredicts stiffness, probably because it does not take into account micro-plasticity occurring during measurements.

Keywords: Porous material; Titanium; Powder processing; Freeze-casting; Mechanical properties

1. Introduction

Titanium-based foams exhibit high strength, low stiffness, low density, high corrosion resistance, and surface oxide biocompatibility, which make them promising for use in medical implants and other technological applications [1–4]. Methods for titanium foam production are based on powder metallurgy and use solid space-holders, creep expansion of trapped gas, partial sintering of powders, or partial powder melting with electron beam and laser [5–14]. All these methods result in equiaxed pores, but there is interest in creating aligned, elongated pores for bone implant applications, which mimic more accurately the bone anisotropic pore structure and mechanical properties, and may allow for better control of bone ingrowth within the foam. Elongated pores in titanium can be created by the anisotropic expansion of entrapped argon in solid titanium [2,6,15]. In another method, titanium powders mixed with powders of a ductile organic filler are extruded, resulting in high aspect ratio pores after removal of the elongated filler and powder sintering [16,17]. In a related method, steel wires are embedded within titanium by powder metallurgy and subsequently electrochemically removed [18]. Aligned elongated pores can also be achieved by the lotus/GASAR technique, where titanium is unidirectionally solidified in a hydrogen/argon atmosphere [19,20]. This method is difficult given the extreme reactivity and tendency for contamination of molten titanium. A related method operating at much lower temperature is directional freeze-casting (also called ice templating), which has recently been used to create elongated pores in titanium [21], as described in more detail below.

In directional freeze-casting [22–24], a powder is dispersed in water (or in another liquid) and the aqueous slurry is then subjected to directional solidification, during which solid ice dendrite grows along the temperature gradient while rejecting the powders into interdendritic regions which freeze at a later point. The ice is then removed by freeze-drying, leaving aligned, elongated sheet-like pores replicating the shape of the ice dendritic crystals, separated by walls of tightly packed powders. Finally, sintering is performed at a temperature sufficiently high to densify the powders within the walls, but low enough to prevent sintering of the large, elongated pores produced by the

* Corresponding author. Tel.: +1 847 491 5370.
E-mail address: dunand@northwestern.edu (D.C. Dunand).

1359-6454/$36.00 © 2010 Acta Materialia Inc. Published by Elsevier Ltd. All rights reserved.
doi:10.1016/j.actamat.2010.09.019

ice dendrites. This method has been demonstrated for hydroxyapatite and collagen, both found naturally within the human body, and for numerous technical ceramics. Investigations have also been performed on the effects of freezing rate, powder loading, and the use of an organic binder [25–30]. Directional freeze-casting with metal powders has, to our knowledge, only been reported by Chino and Dunand [21], who produced titanium foams with aligned, elongated pores whose structure was subsequently studied by tomography by Fife et al. [31]. However, these foams exhibited signs of brittleness in compression because of the very high oxygen content (3.4 wt.%) of the as-received titanium powders, which was due to the small size and high surface area of the powders. In bulk titanium, oxygen in solid solution increases the strength but decreases tensile ductility, reaching near-zero values for ~0.8 wt.% O [32–35]. Recently, Yook et al. freeze-cast, in a non-directional manner, slurries of titanium hydride in liquid camphene to produce low-oxygen titanium foams with equiaxed pores following camphene evaporation, hydride decomposition and titanium sintering [36–38].

In the present study, we demonstrate that directionally freeze-cast titanium foams can be produced from aqueous slurries of commercial metallic Ti powders with an oxygen content low enough to be ductile in compression. We investigate the effects of sintering condition and powder size on the foam structural and mechanical properties. Also, we demonstrate titanium foams exhibiting elongated porosity which is radially (rather than longitudinally) oriented, by modifying the solidification conditions.

2. Experimental procedures

Three commercially available unalloyed titanium powders with irregular shape were used. They were finer in size and much lower in oxygen content than those in our previous study [21], where irregularly shaped powders with a size range of 20–45 μm and a very high oxygen content of 3.4 wt.% were used. Powder A, procured from Atlantic Equipment Engineers (Bergenfield, NJ), had an average particle size <20 μm and an oxygen content of 0.69 wt.%. Powders B and C, both purchased from Phelly Materials (Bergenfield, NJ), which provided mesh sizes of −325 and −500, respectively, had average particle sizes of 20 and 10 μm, with oxygen content of 0.42 and 0.68 wt.%, respectively. All powder oxygen concentrations were determined by ATI Wah-Chang (Albany, OR). Thus, powder sizes (10 and 20 μm) and oxygen contents (~0.4 and ~0.7 wt.%) were varied among samples.

For all experiments, 4.9 g of titanium powder was mixed with 3.0 cm^3 of de-ionized water, which had been degassed under vacuum and into which 0.2 wt.% agar binder (Eden Foods Inc., Clinton, MI) had been dissolved. The resulting slurry, containing 22 vol.% titanium powders, was poured into a cylindrical glass vessel, with 13 mm inner diameter, 1.2 mm average side thickness, 0.93 mm average bottom thickness, and 38 mm height. The slurry was cooled to a few degrees above the freezing point of water, at which point it was mixed to suspend the powders homogeneously within the water. The flat bottom surface of the vessel was then placed in contact with a copper block within a freezer maintained at −5 °C. To encourage directional solidification, the sides and top of the vessel were insulated with polystyrene foam. The vessel was kept in the freezer for at least 3 h to ensure complete solidification of the slurry. The frozen ice/titanium billet, about 37 mm in height, was removed from the vessel and its ice was sublimated for 24 h in a freeze-dryer, operating at a 0.06 torr vacuum at −40 °C. The resulting green titanium billet was then sintered under high vacuum with a maximum residual pressure of 6×10^{-6} torr. After a pre-sintering step at 1000 °C for 2 h, the billet was sintered at 1150 °C for either 8 or 24 h, with heating and cooling ramps of 5 °C min^{-1}.

In Experiment 1, a single foam billet was created with the <20 μm powders A for comparison with results reported by Chino and Dunand [21], where powders with 20–45 μm size were used. The billet was cut such that cross-sections parallel and perpendicular to the pore longitudinal direction could be polished and imaged by optical microscopy and scanning electron microscopy (SEM). Three cylindrical compression specimens were obtained by electro-discharge machining (EDM), with a 2:1 height/diameter ratio and 3–3.5 mm diameter. The height of the specimens was parallel to the freezing direction (longitudinal pore direction) for one and perpendicular for the other two specimens. These two specimens were cut neither parallel nor perpendicular to each other, due to space restrictions. Compression tests were performed at room temperature with a screw-driven load frame at a strain rate of $\sim 10^{-3}$ s^{-1}, using cross-head displacement to determine strain after correction for load–strain compliance and calibration with a sample of known stiffness.

In Experiment 2, three foam billets, one for each powder type (A–C), were created to investigate the effects of powder size, powder oxygen content, and sintering time. Each billet was sintered for 8 h and cut longitudinally in half; one half was retained while the other was sintered for an additional 16 h. Generally, the same procedures were used as for Experiment 1, with the following differences. A single compressive testing specimen was machined by EDM from each half of the billets (with the exception of half billet C sintered for 24 h where material was insufficient), with square cross-section, a 2:1 height/side ratio (with 3–3.25 mm side) and a height parallel to the freezing direction (longitudinal pore direction). After yield, unloading–loading cycles were performed at 10% strain intervals.

In Experiment 3, two billets with radially aligned pores were created using powder B to demonstrate the range of pore architectures achievable by the freeze-casting method. A first billet was frozen in a stainless steel tube (35 mm inner diameter, 0.85 mm wall thickness and 63 mm height). The ends of the vessel were insulated with polystyrene foam while its side was left exposed to the ambient air of the freezer (−19 °C) to promote radial solidification. A second

billet was solidified in a quartz tube (31 mm inner diameter, 1.2 mm thickness, and 55 mm height) with ends insulated as above, which had been frozen into a block of ice maintained at −19 °C. A small adjustment to the slurry was made: 38 g of titanium powder was mixed with 3 cm^3 of de-ionized, vacuum-degassed water containing 0.2 wt.% agar, resulting in a 23.5 vol.% titanium powder slurry. To ensure complete solidification of these larger samples, the vessel was left in the freezer at about −20 °C for >12 h. The same sublimation and pre-sintering steps were used and final sintering was for the lesser time of 8 h.

Total porosity was measured by the Archimedes method, using de-ionized water after coating the sample with a thin layer of grease to prevent ingress of water in the pores. Closed porosity was determined using helium pycnometry and open porosity was calculated as the difference between total and closed porosity. For these calculations, a monolithic titanium density of 4.507 g cm^{-3} was used.

Optical micrographs were used for measurement of pore size and fraction, performed on 45 micrographs with 300× magnification, using the image analysis software Image J. For each specimen, nine optical micrographs were also used to determine micro- and macro-porosity. This was accomplished using the point-count method (ASTM E 562-05) where a grid of 35 equidistant points is placed over an optical micrograph and the number of points contacting a micro-pore, macro-pore, or a titanium wall is recorded.

3. Results

3.1. Foam processing and composition

Three experiments were conducted with powder B to determine the velocity of ice-growth during directional solidification at −5 °C. The height of the ice/slurry interface was measured using a thin alumina rod at ~15 min intervals to a height of 30 mm, corresponding approximately to the height of actual specimens. The interface growth velocity was fast for the first 8 mm of growth but, by 10 mm, had leveled off to an average freezing velocity of 3.0 ± 0.1 μm s^{-1}.

During all experiments, variation in powder distribution along the length of the frozen ice–Ti composites was observed. A thin (<3 mm) layer of pure ice was visible at the very top of the specimen, below which a layer with less Ti was visible, indicating that powder settled in the water before the specimen was fully frozen. As a result, all samples described here are from material outside the bottom or top ~10 mm of the billets.

The oxygen content of the green foams, after ice sublimation but before vacuum sintering, is listed in Table 1. The average increase in oxygen concentration for the three types of powders is 0.08 wt.%, resulting in total oxygen contents of 0.49–0.79 wt.%, depending on original powder oxygen concentration. These concentrations are below or at the critical value of ~0.8 wt.% O for loss of tensile ductility in bulk titanium. This result is encouraging, since it was previously feared [21] that powders finer than about 40 μm would exhibit high levels of oxygen contamination after the extensive exposure to water needed for the freezing step.

Table 1
Oxygen content of powders, preforms and sintered foams with longitudinal pores.

Experiment	Specimen	O content (wt.%)		
		As-received powder	Freeze-dried preform	Sintered foam
1	A-8′	0.69	–	0.84
2	A-8	0.69	0.75	1.1
	A-24	0.69	–	1.0
	B-8	0.41	0.49	0.86
	B-24	0.41	–	0.92
	C-8	0.68	0.79	1.1

As shown in Table 1, the oxygen content of the three foams produced in Experiment 2 increases by 0.3–0.4 wt.% after vacuum sintering, to 0.84–1.10 wt.%. This is the same increase observed previously for foams freeze-cast with somewhat coarser powders with much higher initial oxygen content [21]. This contamination could be further reduced by using a higher vacuum with getters, and by insuring that the freeze-dried preforms are completely devoid of air and/or water. In fact, the foam from Experiment 1 resulted in a total oxygen increase from as-received powder to sintered foams of only 0.15 wt.%. Also, increasing sintering time from 8 to 24 h for foams A and B resulted in near-zero changes in oxygen content (Table 1), indicating that most of the oxygen increase occurs during the initial sintering step, when the foams have high surface area and may contain small amounts of adsorbed air and/or water. As expected, the finest powders C show the highest oxygen content after both freeze-drying and sintering steps, but the increase is small, considering that their specific area may be almost ten times higher than for powders A and B.

In summary, specimens created here with low-oxygen titanium powders exhibited 0.84–1.10 wt.% O, which is somewhat higher than the target value of 0.8 wt.% but much lower than the value of 3.8 wt.% reported by Chino and Dunand [21] in foams using powders with much higher initial oxygen content.

3.2. Foam microstructure

Optical micrographs show longitudinal (Fig. 1a and b) and transverse (Fig. 1c and d) cross-sections of foam A-8 at low and high magnifications. Macro-pores replicating the plate-like shape of the ice dendrites are separated by titanium walls, as also reported previously for somewhat larger titanium particles (20–45 μm) [21]. In the longitudinal section (Fig. 1a), the walls are parallel to each other and aligned with the main dendrite growth direction. In the transverse cross-section (Fig. 1c), walls are parallel

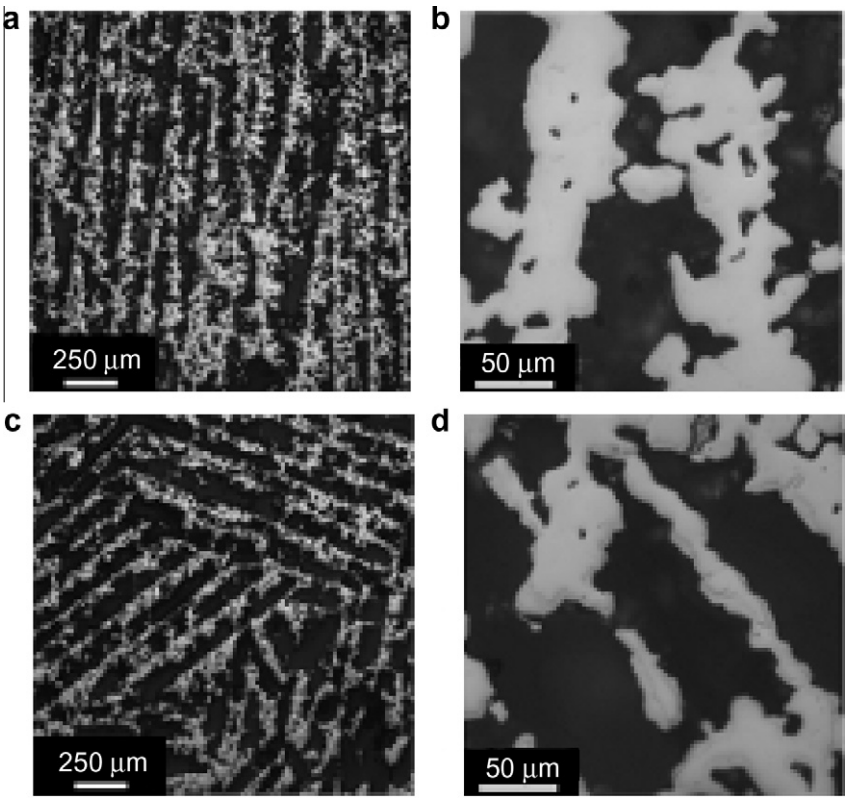

Fig. 1. Optical micrographs of foam A-8 (44.6% porosity). (a and b) Longitudinal cross-sections, at low and high magnification; (c and d) transverse cross-sections, at low and high magnification. Titanium is white and pores are black.

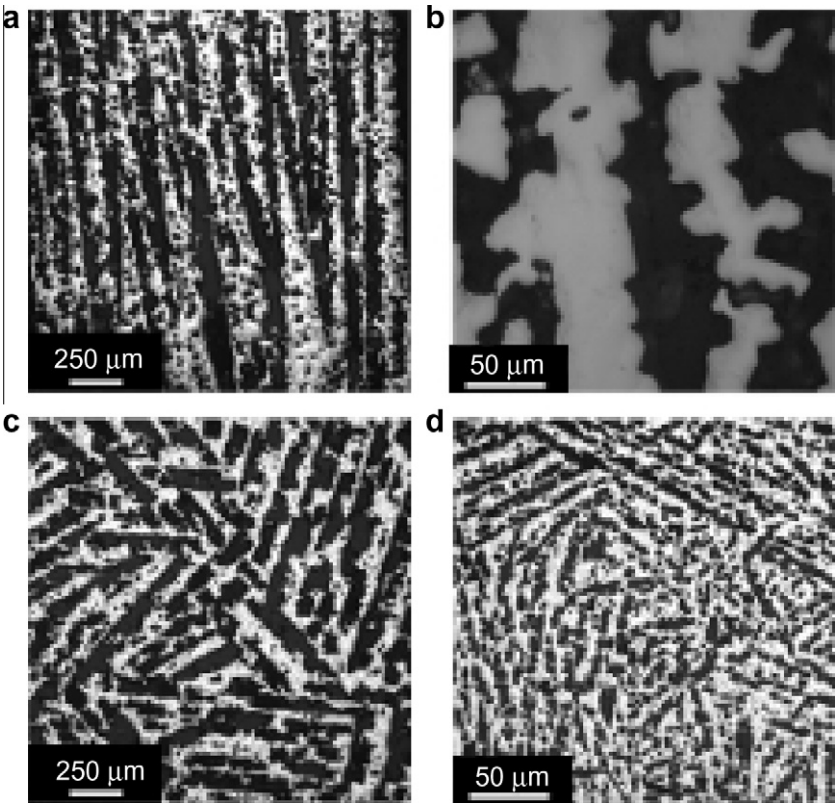

Fig. 2. Optical micrographs of foam A-24 (37.4% porosity). (a and b) Longitudinal cross-sections, at low and high magnification; (c and d) transverse cross-sections, taken from (c) top and (d) bottom of billet at low magnification.

within regions a few square millimeters in area, which probably represent individual ice grains, nucleated at the bottom of the sample and containing colonies of parallel dendrites. These changes in wall orientations are reflected in the longitudinal cross-section (Fig. 1a) as regions where macro-pores and walls have varying apparent widths.

The higher magnification micrographs in Fig. 1b and d show the structure of the walls, which consist of sintered titanium particles. The sintering is sufficiently advanced that individual powder particles cannot be identified, but is still incomplete as small pores are visible within the walls and the wall surface remains jagged (Fig. 1b and d). Two populations of pores are thus present in the foams: (i) macro-pores resulting from the ice dendrites, which are plate-like in shape, parallel to the solidification direction, interconnected to each other through occasional fenestrations across walls, and open to the foam surface; and (ii) micro-pores within the titanium walls, which result from incomplete sintering of the titanium powders.

Dendritic macro-pores are also clearly visible in Fig. 2a, a longitudinal optical micrograph of foam A-24. The longer sintering time reduced the amount of micro-porosity within the titanium walls (Fig. 2b), with no visible effect on the size and shape of the macro-pores. Transverse sections taken from billet upper (Fig. 2c) and lower (Fig 2d) regions have similar microstructures but on different length scales. There are two reasons for this difference in feature size. The first is that the solidification rate decreases with distance from the heat sink (this effect is visible but small in the quasi-linear region past the first 10 mm) and a lower solidification rate leads to larger dendrites, and thus larger replicated macro-pores [23,24,26]. The second is that a gradient in powder density exists in the slurry before solidification due to powder settling, as discussed previously. Both of these effects result in a foam structure which is denser and has narrower macro-pores at the bottom of the billet.

Decreasing powder size from 20 to 10 μm while using the same sintering time resulted in a microstructure with denser walls (Fig. 3), visible in high magnification micrographs (Fig. 3b). Decreased micro-porosity indicates that densification by sintering occurred more completely for the smaller powders, as expected from their higher surface-to-volume ratio and the shorter diffusion distances. An additional mechanism for the improved sintering of the finer powders may also be operating: given that the wall width is not much larger than the coarser, 20 μm powders used here, finer 10 μm powders will pack more densely than coarser powders, since a smaller fraction are at the dendrite–wall interface where packing is less efficient. Transverse cross-section micrographs in the upper and lower regions of the C-8 billet (Fig. 3c and d, respectively) again show the effects of solidification rate and powder settling on macro-pore size, as discussed previously for Fig. 2c and d.

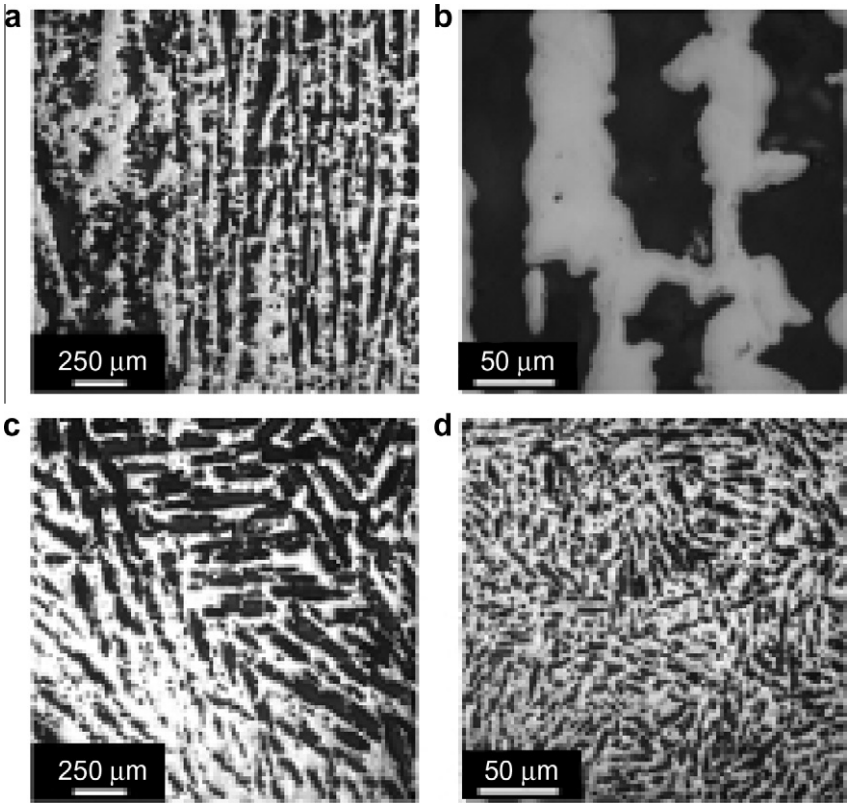

Fig. 3. Optical micrographs of foam C-8 (41.5% porosity). (a and b) Longitudinal cross-sections, at low and high magnification; (c and d) transverse cross-sections, taken from (c) top and (d) bottom of billet.

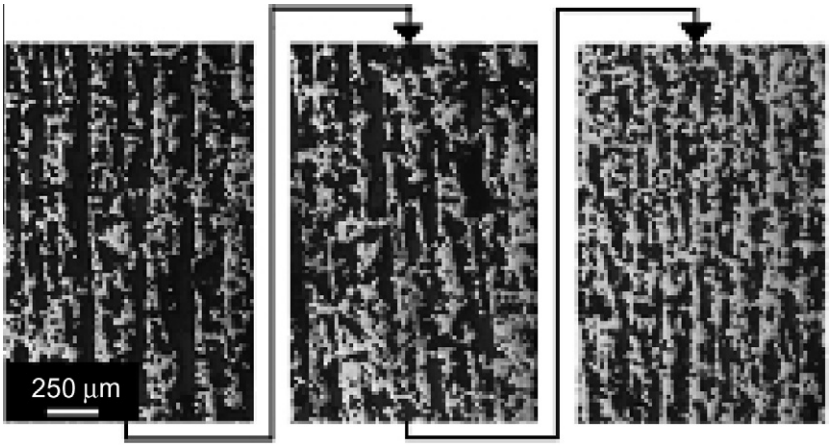

Fig. 4. Optical micrographs of longitudinal cross-sections of foam B-8 (51.3% porosity) from top (left) to middle (center) to bottom (right) of billet.

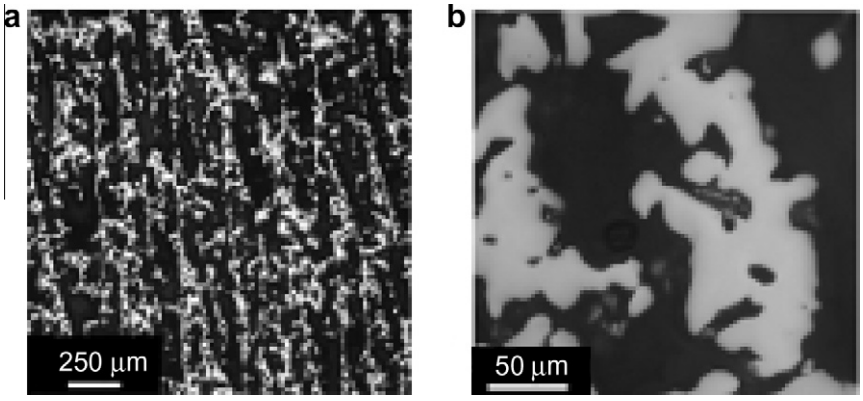

Fig. 5. Optical micrographs of longitudinal cross-sections of foam B-24 (46.9% porosity) at (a) low and (b) high magnification.

The increase in wall thickness from the bottom to the top of a foam billet is further illustrated by longitudinal micrographs from the top, middle, and bottom of the B-8 billet presented in Fig. 4. Near the ingot bottom, the titanium walls are denser and thicker and the dendritic macro-pores are thinner than near the top. Finally, Fig. 5a and b shows a longitudinal micrograph for the most porous sample B-24. These micrographs illustrate that the increase in porosity is derived mostly from an increase in micro-porosity within the titanium walls as opposed to macro-porosity between the titanium walls.

The average macro-pore width, measured on optical micrographs of longitudinal cross-sections, is given in Table 2 for all foams. The large error bars are indicative of the wide variation in macro-pore width, both along the length of individual pores and among different pores. Furthermore, plate-like pores may appear broader on cross-sections, when their surface normals are not parallel (or perpendicular) to the cross-section; in fact, only three-dimensional reconstructions can provide accurate pore widths, as done recently on the present freeze-cast titanium foams [31]. Table 2 that the macro-pores in the present foams approach, and may even achieve in some cases, the value of 100 μm, which has been demonstrated by various studies to be the minimum pore size for bone in-growth into implants [39–41]. Wider macro-pores can be produced by lowering the initial powder content in the slurry and/or by reducing the freezing rate. Also, Yoon et al. [42] showed that dendrites in freeze-cast alumina–ice billets could be coarsened after solidification, resulting in a 10- to 20-fold increase in dendrite size. This approach, which necessitates particle pushing by the coarsening dendrites, may however be difficult to achieve in the present case, given the relatively

Table 2
Apparent width of dendritic macro-pores in freeze-cast specimens measured on longitudinal cross-sections.

Specimen	Pore width [μm]
A-8	61 ± 20
A-24	57 ± 18
B-8	70 ± 32
B-24	64 ± 25
C-8	50 ± 17
Average	60 ± 24

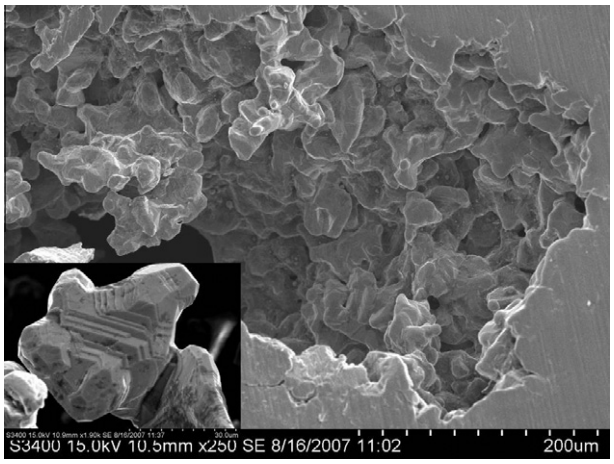

Fig. 6. SEM micrograph of foam A-8 (44.6% porosity) cross-section, showing a macro-pore surrounded by titanium walls with high roughness. Higher magnification inset shows faceting and neck between two partially sintered powder particles.

coarse size of the titanium powders, which is necessary to maintain low oxygen contamination and reactivity with water.

Fig. 6 shows an SEM micrograph of foam A-8, with a high depth of field permitting a three-dimensional assessment of the surface of the walls. It is apparent that the incomplete sintering leading to the micro-pores visible with both optical microscopy and SEM also results in high roughness of the macro-pore walls. This may reduce the stiffness and strength of the walls, while also decreasing their fatigue resistance. However, pore roughness has been found to improve bone in-growth [43,44]. The inset of Fig. 6 shows two titanium powders connected by a sintering neck displaying submicron facets. Faceting of the titanium powders, which is present throughout the sample, has

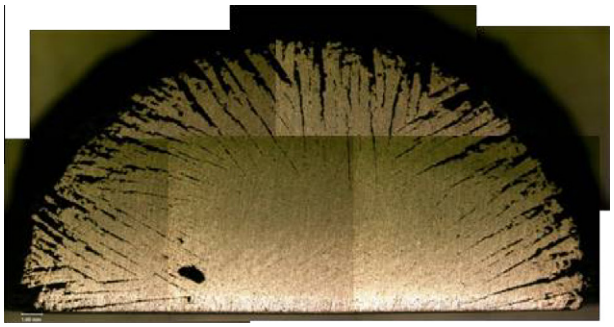

Fig. 7. Optical micrograph montage of transverse cross-sections of billet C (frozen in stainless steel tube). Large radially oriented pores (visible to the naked eye) are present along the entire circumference of the billet (one half shown here).

been observed previously in titanium foams subjected to long sintering times, and was explained by the anisotropy of the surface energy of titanium [6].

Fig. 7 shows one half of the transverse cross-section of the foam produced by radial freezing (Experiment 3) in a stainless steel tube. Elongated pores are present along the whole circumference of the specimen and are generally, but not exactly, aligned with the radial temperature gradient. Pores in the foam created by radial freezing in a quartz tube showed the same orientation, but a much finer width. A radial cross-sectional strip of this foam is shown in Fig. 8a, from which three porous regions are apparent. Near the outer surface of the billet in contact with the heat sink, pores are near equiaxed (Fig. 8b), as expected from the rapid slurry freezing preventing the formation of aligned dendrites. Further from the heat sink (Fig. 8c), elongated pores are aligned radially along the temperature gradient, clearly replicating directionally solidified ice dendrites. These elongated pores are wider near the billet

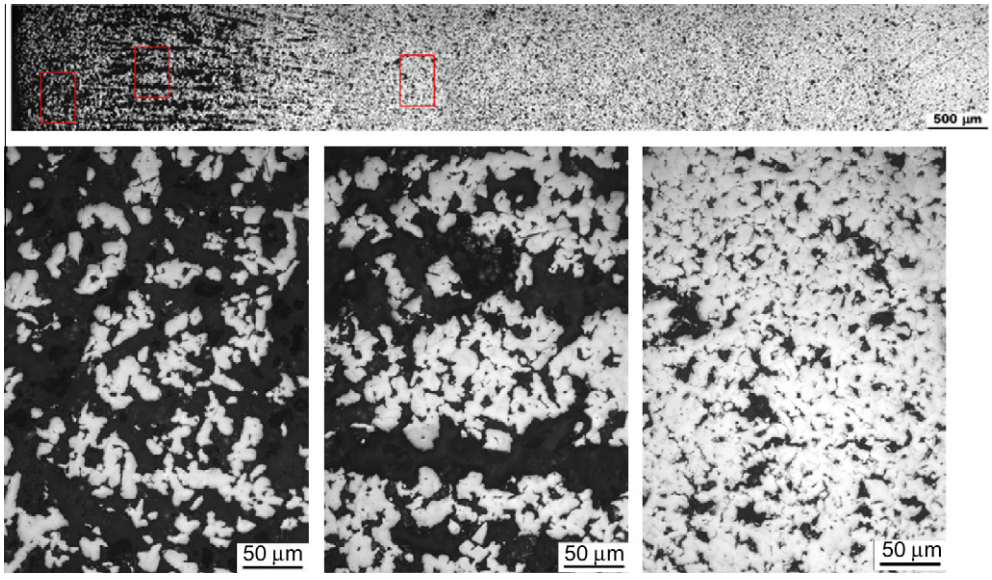

Fig. 8. Optical micrograph montage showing radial strip for billet C (frozen in quartz tube) extending from billet edge (left) to center (right). Higher magnification micrographs are shown for edge, dendritic section, and center of billet.

Table 3
Foam porosity determined (i) from density measurements with total and closed values determined respectively by the Archimedes method and helium pycnometry (errors are standard deviation); and (ii) from point-count method on metallographic cross-sections for macro- and micro-porosity (error are 95% confidence interval).

	Density measurements		Metallographic measurements		
	Total porosity (%)	Closed porosity (%)	Total porosity (%)	Macro-porosity (%)	Micro-porosity (%)
A-8′	52.7 ± 0.3		–	–	–
A-8′ L1[a]	55.0 ± 0.4		–	–	–
A-8′ L2[a]	52.4 ± 1.2		–	–	–
A-8	44.6 ± 0.6	1.6 ± 6.0	45 ± 7	34 ± 9	12 ± 3
A-24	37.4 ± 0.9	0.7 ± 5.8	38 ± 10	32 ± 11	6 ± 4
B-8	51.3 ± 0.7	-1.0 ± 8.7	56 ± 8	44 ± 11	12 ± 5
B-24	46.9 ± 1.1	-1.2 ± 7.4	47 ± 13	36 ± 10	11 ± 6
C-8	41.5 ± 0.8	3.2 ± 5.4	34 ± 7	26 ± 7	8 ± 4
B-8 radial	52.5 ± 0.1	10.9 ± 3.3	–	–	–

[a] Machined with long axis perpendicular to pore orientation.

surface and narrowed toward its center, unlike the pores found in the longitudinally solidified specimens whose width increases with distance from the heat sink. This narrowing of the pore width is likely due to the fact that, as dendrites progress towards the center of the billet, the powder density in the slurry is increasing as a result of powder pushing by the ice front. Finally, as solidification proceeds, the powder density in the slurry reaches a critical value and directional dendrites of pure ice cannot form: this results in a region in the center of the specimen with equiaxed porosity (Fig. 8d).

3.3. Foam density and porosity

Specimen total and closed porosity are listed in Table 3. The total porosity, determined by Archimedes density measurements on machined mechanical testing specimens, has small error bars. The closed porosity determined by helium pycnometry on mechanical specimens indicates that, despite much higher experimental errors, closed porosity is small, and possibly zero, within these samples. These results indicate that the large, dendritic macro-pores, which were originally open to the billet surface when the ice was sublimated, were not subsequently closed during the sintering treatment. Also, the micro-pores within the walls are connected to the macro-pores, possibly due to the relatively small width of titanium walls, as compared to the size of the powders.

Table 3 shows significant variations in total porosity within specimens with the same powder size subjected to the same sintering conditions. All specimens were machined from approximately the same height within the billet so as to minimize the effect upon porosity of powder settling within the slurry. Given these variations, the expected trend of porosity p decreasing with increasing sintering time – i.e., foams A-8 ($p = 44.6\%$) vs. A-24 ($p = 37.4\%$) – cannot be unequivocally confirmed.

Independent measurements of macro- and micro-porosity performed by the point-count method on two-dimensional cross-sections are also reported in Table 3. The error bars are much larger than for the density measurements. Additional uncertainty originates from the difficulty of determining whether a pore is macro- or microscopic: a simple, but somewhat arbitrary, rule was to count as macroscopic any pore with aspect ratio larger than four and length greater than 150 μm. Within the large experimental error, both sets of measurements for the total porosity are in agreement. It is also evident that the micro-porosity (measured from cross-section) is larger than the closed porosity (measured by pycnometry and close to zero), confirming that the micro-porosity within the walls is mostly open.

3.4. Foam compressive properties

3.4.1. Stiffness

Fig. 9 shows, as a function of compressive strain, the compressive stiffness of the foams produced in Experiment 2, as measured during loading/unloading cycles, a method previously used to follow the evolution of damage in metallic foam [45,46]. The stiffness, both on loading and on unloading, first increases and then decreases over the strain

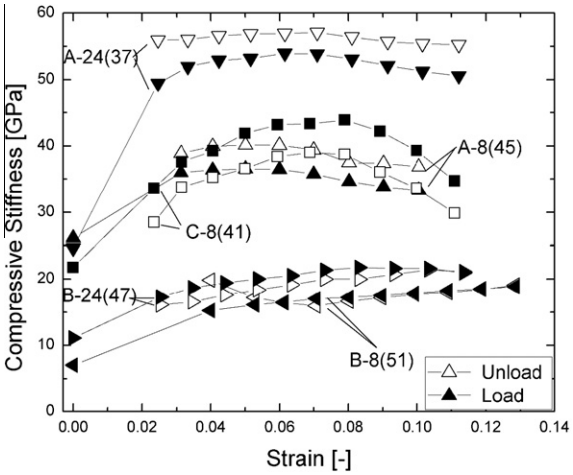

Fig. 9. Plot of compressive stiffness vs. strain for foams from Experiment 2 (with porosity in parentheses) as measured during loading/unloading cycles.

range 0–0.13. Also plotted at 0% strain in Fig. 9 are the modulus values measured on the initial loading branch of the stress–strain curves (prior to any unloading), which are markedly below the peak stiffness. The presence of a peak stiffness at intermediate strains can be explained by a competition between densification which increases the stiffness of the foam, and damage which decreases it. The first mechanism becomes exhausted as strain increases while the second becomes amplified. Hereafter, the average of the first loading and unloading stiffness values determined at ~2% strain is used to describe the foam's stiffness.

3.4.2. Plastic deformation

For all compression tests conducted parallel to the dendrite direction, three different types of stress–strain curves were observed, as illustrated in Fig. 10 where the load–unload loops are removed to ease viewing of the curves. Four of the six tested specimens exhibited a stress–strain curve qualitatively similar to that of foam A-24 ($p = 37.4\%$) shown in Fig. 10. This foam exhibits an initial elastic region, a yield point, a peak stress, followed by a stress drop spreading over a sizeable strain interval. This is followed by an extended plateau where stress fluctuates, which is terminated by a stress increase due to densification (in some cases failure occurs before this stage). The magnitude of the stress drop depends on the peak stress, but the plateau region is consistently in the 200–300 MPa range. In one case, characterized in Fig. 10 by foam B-8 ($p = 51.3\%$), there is no stress drop and the broad plateau is reached smoothly, and eventually leads to densification. Another exception is foam A-8′ ($p = 52.7\%$), which suffered a damage event so serious that the specimen fractured into two separate pieces with the load dropping to zero before densification could occur. The specimens resulting in these last two uncharacteristic curves had the highest porosities and lowest yield strengths of all mechanically tested foams.

Fig. 11 shows comparisons of stress–strain curves for foams from Experiment 1 (foam A-8′ with $p = 52$–54%) with uniaxial deformation occurring parallel to the freezing direction (one curve) and perpendicular to the freezing direction (two curves). Not surprisingly given the strong notch effect produced by the elongated macro-pores, the foams are weaker when tested perpendicular to the freezing direction. The peak stress, however, remains sizeable (125–150 MPa), as is the energy absorbed during crushing (as measured by the area under the stress–strain curve). Also plotted in Fig. 11 are longitudinal and transverse compressive curves for titanium foams created previously by Chino and Dunand [21] from Ti powders with much higher oxygen content: they all show much reduced strength and energy absorption. This may be partially due to the higher porosity of these foams (61% vs. 52–54%), but it is likely that the main effect is the decreased ductility of the Ti walls from the high oxygen content.

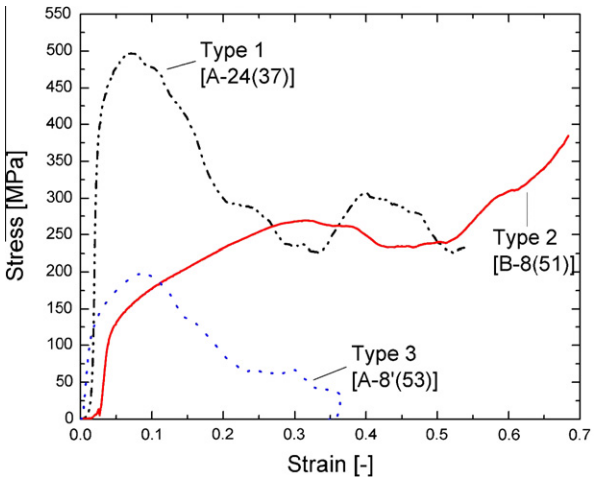

Fig. 10. Compressive stress–strain curves for foams A-24, B-8, and A-8′ (37.4%, 51.3%, and 52.7% porosity, Experiment 2).

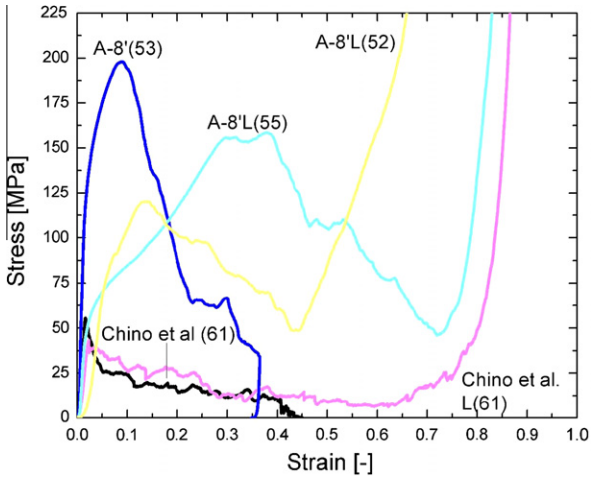

Fig. 11. Compressive stress–strain curves for foams from Experiment 1 for loading occurring parallel to dendritic pores (A-8′ with 52.7% porosity) and perpendicular to dendritic pores (A-8′ L1 and L2 with 55 and 52.4% porosity).

Finally, the mechanical properties of foams are expected to be isotropic in all directions perpendicular to the freezing direction, given that the ice dendrites, while aligned in the vertical direction, grow in colonies showing multiple, uncorrelated orientations in the horizontal direction (Figs. 1–3). The two perpendicular curves in Fig. 11 show roughly the same peak stress, despite having been cut from the billet with their longitudinal directions at different angles.

4. Discussion

4.1. Microstructure

As compared to freeze-casting experiments of ceramics which use sub-micrometer powder particles, the 10–20 μm titanium powders used here are much coarser. Decreasing their size further would be desirable to reduce settling in the slurry, to improve the particle pushing by the ice dendrites leading to better packing in the interdendritic spaces, and to reduce sintering time and/or temperature. Titanium

powders finer than those used here are however likely to exhibit unacceptably high oxygen contents from exposure to air and water during the freeze-casting process. While this issue could be minimized by using cover gas and/or non-oxidizing fluids for the freeze-casting (e.g., hydrocarbons such as camphene or naphthalene [36,47,48]), the 10–20 μm titanium particle size used here is sufficiently fine to permit the relatively slow freezing rates without excessive settling which leads to coarse dendrites, and after freeze-drying and sintering, wide macro-pores useful for medical implants.

For a given particle size, there is a critical freezing velocity below which particles are pushed by the growing dendrites and above which they are engulfed by them [30,49]. This critical velocity has previously been calculated [21] for the titanium/water system by considering a force balance between the viscous drag resulting from the pushing of the particle by ice which favors entrapment, the repulsive molecular interaction at the particle/ice interface which favors pushing, and the gravitational force acting on the particles. For titanium particles with diameters of 10 and 20 μm, these critical velocities are 75 and 37 μm s^{-1} [21], respectively, and are thus well above the freezing velocities of 3 μm s^{-1} used here. This is in agreement with the observation that, for all specimens, the particles were pushed into the interdendritic space by the growing ice dendrites.

4.2. Foam compressive properties

Modeling of the mechanical properties for the freeze-cast titanium foams is made difficult by their complex microstructure: long, aligned open macro-pores separated by aligned walls which contain closed micro-porosity and show rugged surface features. As a first point of comparison, the Gibson–Ashby equations can be used, which however assume a very different foam architecture: equiaxed cells with struts deforming by bending. Furthermore, these equations (labeled GA in the following) were developed for higher porosity materials which have the same yield strength and peak strength. The yield/peak strength and the Young's modulus of the foams are derived [50] as:

$$\sigma^*_{GA} = \sigma_{Ti} C_1 \left(\frac{\rho^*}{\rho_{Ti}}\right)^{3/2} \left(1 + \left(\frac{\rho^*}{\rho_{Ti}}\right)^{1/2}\right) \tag{2}$$

$$E^*_{GA} = E_{Ti} C_2 \left(\frac{\rho^*}{\rho_{Ti}}\right)^{2} \tag{3}$$

where σ_{Ti} and E_{Ti} are the yield strength and Young's modulus of dense titanium, ρ^* and ρ_{Ti} are the density of the porous and dense titanium, and C_1 and C_2 are constants experimentally determined as 0.23 and 1, respectively, for foams with higher porosity than the present ones.

The simplest possible model taking into account the aligned, plate-like structure of the macro-pores in the present foams considers dense titanium walls perfectly aligned in the direction of the applied stress and extending over the entire height and width of the specimen. Then, the "rule of mixtures" (ROM in the following) can be used:

$$\sigma^*_{ROM} = \sigma_{Ti} \left(\frac{\rho^*}{\rho_{Ti}}\right) \tag{4}$$

$$E^*_{ROM} = E_{Ti} \left(\frac{\rho^*}{\rho_{Ti}}\right) \tag{5}$$

We now combine the GA and ROM equations to create a new model, with a microstructure closer to that exhibited by the present foams. First, the GA equation (Eqs. (2) and (3)) are used to describe the properties of the wall material containing equiaxed micro-pores. Second, the ROM equations (Eqs. (4) and (5)) are used to model the parallel walls (with GA-derived strength and stiffness due to micro-porosity) separating the aligned macro-pores. Combining Eq. (2) with Eq. (4), and Eq. (3) with Eq. (5) results in the following equations (labeled GAR, standing for Gibson–Ashby–ROM, in the following):

$$\sigma^*_{GAR} = \sigma_{Ti} C_1 \left(\frac{(1-p)^{3/2}}{(1-p_M)^{1/2}}\right) \left(1 + \left(\frac{1-p}{1-p_M}\right)^{1/2}\right) \tag{6}$$

$$E^*_{GAR} = E_{Ti} C_2 \left(\frac{(1-p)^{2}}{1-p_M}\right) \tag{7}$$

where p is the total porosity, p_M the macro-porosity and thus $p - p_M$ the micro-porosity. The relative density (ρ^*/ρ_{Ti}) in Eqs. (2)–(5) is given by $1 - p$. These equations are valid only over the limited range of porosity for which the constants C_1 and C_2 were determined.

Measured foam 0.2% yield strength (Fig. 12) and compressive stiffness (Fig. 13) are plotted against porosity. A best-fit power-law line was calculated using only those specimens whose compression directions are parallel to the freezing direction, demarcated with solid symbols in Figs. 12 and 13. Predicted values using the GA, ROM and GAR models, using the experimental total and macro-porosity values, are included as hollow symbols. Error bars in the vertical and horizontal axes reflect the uncertainty in the total porosity and micro-porosity measurements, respectively. Because the yield strength of titanium is dependent on the oxygen content (Section 3.4), different values for σ_{Ti} are used for each foam based on its measured oxygen content. A literature review reveals sufficient data [32–35] to determine a linear relationship between oxygen content c_O and yield strength σ_{Ti} as shown in Fig. 14:

$$\sigma_{Ti}\ (\text{MPa}) = 201 + 921 c_O(\text{wt.}\%) \tag{8}$$

Using the average values of micro-porosity for the six specimens, lines representing predicted values for each of the three models are also shown in Figs. 12 and 13, as discussed below.

The ROM strength predictions are an upper bound which is unlikely to be approached experimentally, given that it assumes perfectly aligned, smooth, fully dense walls unable to buckle: none of these assumptions applies to the

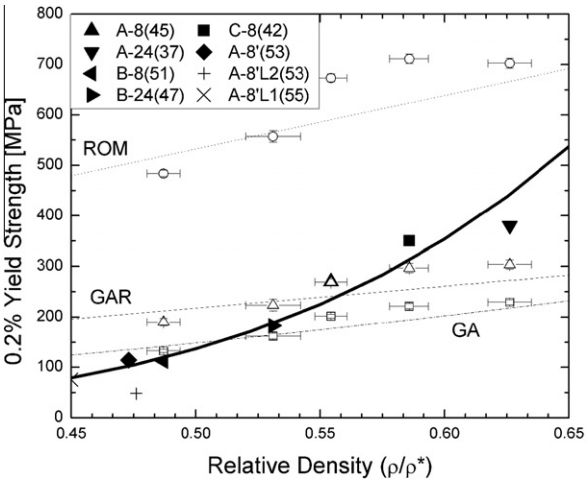

Fig. 12. Plot of compressive yield strength vs. relative density showing measured foam data and model predictions.

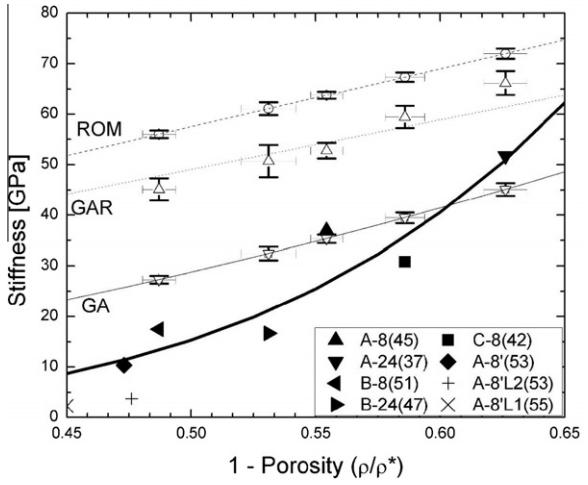

Fig. 13. Plot of compressive stiffness vs. relative density showing measured foam data and model predictions (Eqs. (2)–(7)).

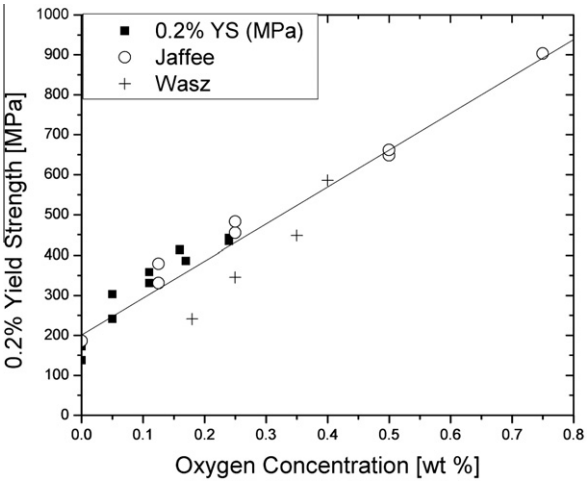

Fig. 14. Plot of tensile yield strength vs. oxygen content for bulk titanium with literature data gathered from Refs. [32,33,35]. Best fit line is given by Eq. (8).

present foams. The experimental values for the foam yield stress are in rough agreement with the GAR model for the four highest densities, with a trend showing a steeper increase (a higher exponent for the power-law) than given by this model. The elastic modulus data (Fig. 13) show the same steep trend, but with experimental values much lower than predicted, even by the most compliant GA. This discrepancy may indicate a systematic underestimation of the experimentally measured compressive stiffness due to the large stress range needed to determine a slope on a stress–strain curve: micro-yielding and localized plasticity on both loading and unloading may occur, thus mimicking as elastic deformation and leading to systematically low apparent compressive stiffnesses. The yield strength, on the other hand, is a measure of the macro-yielding of the foam and is much less affected by micro-yielding or -damage that may be occurring in the linear portion of the stress–strain curve.

The steep increases in stiffness and strength of the foam with increasing density may reflect the fact that micro-porosity is eliminated preferentially to macro-porosity during sintering. Elimination of the micro-porosity increases more strongly strength and stiffness than does elimination of macro-porosity (as visible by the exponents of 1.5 and 2 in Eqs. (2) and (3) vs. 1 in Eqs. (4) and (5)). It is thus expected to lead to rapid gain in these properties. This is true even as total porosity remains constant in the case when micro-porosity decreases by sintering of the walls while macro-porosity increases due to the thinner walls. In fact, however, the total porosity decreases as the macro-pores also shrink during sintering, so the effect of sintering on the mechanical properties is stronger.

While non-biomedical applications exist for titanium with aligned, elongated macro-pores (e.g., structural core of sandwiches, filters, and heat exchangers), the main application pursued in the present study is for permanent bone implant material. To reduce stress shielding, such implants must have a low stiffness, approaching that of bone, and a high strength, to prevent fatigue-driven failure. The present foams have the desired characteristics of low stiffness (10–52 GPa) and high yield strength (110–380 MPa) in the longitudinal macro-pore direction, which can be tuned by varying porosity: the porosity range of 37–53% studied in the present study can be further expanded if needed. If much lower stiffnesses are desired, the foams can be used with porosity aligned at 90° (or any non-zero) angle with respect to the applied load, but this leads to a strength decrease, as shown in Fig. 11.

4.3. Foam energy absorption

Beside the smoothness (absence of serrations) of the stress–strain curve and absence of sample splitting or spalling, a measure of compressive ductility for a metallic foam is given by the crushing energy per unit mass, corresponding to the area under the stress–strain curve up to densification. As visible in Figs. 10 and 11, the stress fluctuates

significantly in the plateau region, indicative of distinct damage and crushing events during deformation. Published stress–strain curves for titanium foams with 80% isotropic pores [51] exhibit a smooth plateau without peak stress, but with decreasing porosity, a stress drop appears and the smoothness of the plateau region deteriorates. Furthermore, Park and Nutt [52] show that foams with a distribution in pore shape and size lead to a post-yield stress-drop and a highly fluctuating plateau region. Not only do the present foams have relatively low porosity and wide pore size and shape distributions, but their highly elongated macro-pores may elastically or plastically buckle, leading to a sharp stress-drop.

Here, we integrate the stress–strain curves up to a maximum strain of 50%, since not all foams were deformed to densification, to measure the crushing energy per unit mass. This property, which is of interest for crash, blast or projectile protection, is plotted in Fig. 15 as a function of the stress at a 25% strain (well into the plateau) for the present foams. Data points for the two freeze-cast titanium foams with much higher oxygen content created by Chino and Dunand [21] fit the general trend. This indicates that oxygen affects similarly both strength and crushing energy, as expected since the latter is mostly defined by the former, assuming a smooth densification plateau. Oxygen increases the intrinsic strength of titanium, but decreases its ductility and toughness. Thus, the foam static strength may be improved by oxygen, with the crushing energy increasing in concert. However, in terms of fatigue and damage resistance, it is undesirable for the titanium foam to display high oxygen content. This is the reason for the upper limit of 0.4 wt.% oxygen in dense titanium used commercially in orthopedic applications [53,54]. As shown in Table 1, freeze-dried specimens exhibit 0.49 wt.% O before sintering. Reducing oxygen contamination during sintering, which is possible with getters and improved pumping, will thus lead to foams with oxygen content close to the above requirement.

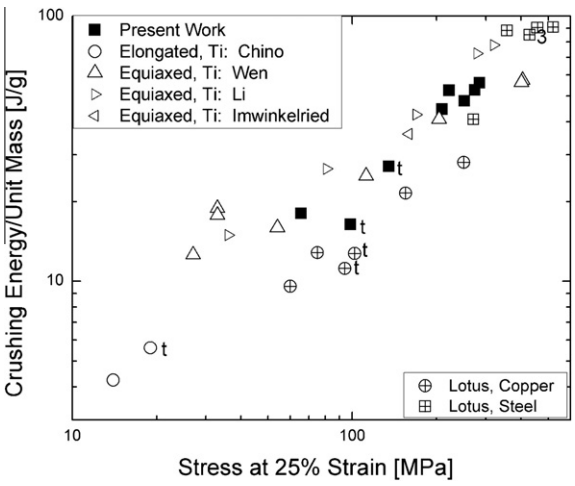

Fig. 15. Plot of compressive energy absorption vs. relative density for present freeze-cast Ti foams, previous freeze-cast Ti foams with higher oxygen content [21], and other Ti foams with equiaxed pores [51,55,56]. Also shown are lotus Cu foams [59–61] and Fe foams [57,58] with elongated pores created by directional solidification of the metallic melt. Foams tested in the transverse directions are marked with the letter *t*.

Fig. 15 shows that energy absorption for a number of titanium foams with equiaxed porosity is somewhat higher, at a given stress (taken here at 25% strain), than for the present titanium foams with elongated pores, probably reflecting the reduced notch effect produced by smooth, equiaxed pores [21,51,55,56]. Finally, energy absorption for lotus steel (with cylindrical pores aligned along the deformation direction) are in line with those for freeze-cast titanium, while data for lotus copper are inferior [57–61]. This probably reflects the much lower density-compensated strength of copper as compared to titanium or steel.

5. Conclusions

Titanium foams with aligned, elongated macro-pores were created by directional freeze casting of aqueous slurries of titanium powders (with relatively low oxygen content of 0.41–0.69 wt.%), followed by freeze drying to remove ice dendrites and sintering to densify the powders into continuous walls. The main results are as follows.

- Microstructure analysis reveals pores on two length-scales: aligned, sheet-like macro-pores produced by removal of the ice dendrites, separated by titanium walls with rugged surfaces and equiaxed micro-pores, due to incomplete sintering of the titanium powders.
- Despite exposing the fine titanium powders (10–20 μm) to water and ice for long times during the freeze-casting process, oxygen contamination is modest (as low as 0.14 wt.%) and the foams exhibit semi-ductile behavior and high energy absorption in compression.
- Foam compressive stiffness is initially low (7–25 GPa), probably due to micro-plasticity. As strain increases, the foam stiffness, measured by load–unload excursions, increases (by a factor ~2) before decreasing. This is assigned to densification of micro-pores and accumulation of damage, respectively.
- A simple model taking into account both types of pores to predict foam stiffness and strength is in general agreement with experimental measurements of strength, but overpredicts stiffness, probably because micro-plasticity is occurring during the measurement.
- The low stiffness, high strength, semi-ductile crushing behavior of these foams makes them attractive as bone implants. Desirable for this application are further decrease in oxygen content, relative density and residual micro-porosity, and increase in pore width, which are achievable by improved processing techniques.

Acknowledgment

This research was supported by the US National Science Foundation though Grant DMR-0505772.

References

[1] Lefebvre LP, Banhart J, Dunand DC. Adv Eng Mater 2008;10(9):775–87.
[2] Spoerke ED et al. J Biomed Mater Res A 2008;84A(2):402–12.
[3] Dunand DC. Adv Eng Mater 2004;6(6):369–76.
[4] Singh R et al. Mater Technol 2010;25:127–36.
[5] Wen CE et al. Scripta Mater 2001;45(10):1147–53.
[6] Kearns MW et al. Int J Powder Metall 1988;24(1):59–64.
[7] Oh IH et al. Scripta Mater 2003;49(12):1197–202.
[8] Krishna BV. Acta Biomater 2007;3:997–1006.
[9] Heinl P et al. Adv Eng Mater 2007;9(5):360–4.
[10] Erk KR, Dunand DC, Shull KA. Acta Mater 2008;56(18):5147–57.
[11] Li CF, Zhu ZG, Liu T. Powder Metall 2005;48(3):237–40.
[12] Cansizoglu O, Harryson O, Cormier D, West H, Mahale T. Mater Sci Eng A 2008;492:468–74.
[13] Murray NGD, Dunand DC. Compos Sci Technol 2003;63(16):2311–6.
[14] Murray NGD, Schuh CA, Dunand DC. Scripta Mater 2003;46(9):879–83.
[15] Davis NG et al. J Mater Res 2001;16(5):1508–19.
[16] Tuchinskiy L. J Adv Mater 2005;37(3):60–5.
[17] Chino Y, Dunand DC. Adv Eng Mater 2009;11(1–2):52–5.
[18] Kwok PJ, Oppenheimer SM, Dunand DC. Adv Eng Mater 2008;10(9):820–5.
[19] Shapovalov V, Boyko L. Adv Eng Mater 2004;6(6):407–10.
[20] Higuchi Y, Ohashi Y, Nakajima H. Adv Eng Mater 2006;8(9):907–12.
[21] Chino Y, Dunand DC. Acta Mater 2008;56(1):105–13.
[22] Zhang H, Cooper AI. Adv Mater 2007;19(11):1529–33.
[23] Deville S, Saiz E, Nalla RK, Tomsia AP. Science 2006;311(5760):515–8.
[24] Deville S, Saiz E, Tomsia AP. Acta Mater 2007;55(6):1965–74.
[25] Araki K, Halloran JW. J Am Ceram Soc 2005;88(5):1108–14.
[26] O'Brien FJ et al. Biomaterials 2004;25(6):1077–86.
[27] Koh YH et al. J Am Ceram Soc 2006;89(12):3646–53.
[28] Lee SH et al. J Am Ceram Soc 2007;90(9):2807–13.
[29] Woinet B et al. J Food Eng 1998;35(4):395–407.
[30] Barr SA, Luijten E. Acta Mater 2010;58(2):709–15.
[31] Fife JL, Li J, Dunand DC, Voorhees PW. J Mater Res 2009;24(1):117–24.
[32] Jaffee RI, Ogden HR, Maykuth DJ. Trans AIME 1950;188:1261–6.
[33] Finlay WL, Snyder JA. Trans AIME 1950;188:277–87.
[34] Jaffee RI. J Met 1955:247–52.
[35] Wasz ML et al. Int Mater Rev 1996;41(1):1–12.
[36] Yook SW et al. Mater Lett 2008;62(30):4506–8.
[37] Yook SW, Kim HE, Koh YH. Mater Lett 2009;63(17):1502–4.
[38] Jung HD et al. Mater Lett 2009;63(17):1545–7.
[39] Xue W et al. Acta Biomater 2007;3(6):1007–18.
[40] Hulbert SF et al. J Biomed Mater Res 1970;4(3):433–56.
[41] Karageorgiou V, Kaplan D. Biomaterials 2005;26(27):5474–91.
[42] Yoon BH et al. Scripta Mater 2008;58:537–40.
[43] Daugaard H et al. J Biomed Mater Res A 2008;87A(2):434–40.
[44] Goyenvalle E et al. In: International symposium on ceramics in medicine. Nantes, FRANCE: Trans Tech Publications Ltd.; 2007.
[45] Despois JF, Mueller R, Mortensen A. Acta Mater 2006;54(16):4129–42.
[46] Lefebvre LP et al. Adv Eng Mater 2006;8(9):841–6.
[47] Koh YH et al. J Am Ceram Soc 2006;89(10):3089–93.
[48] Nyberg E, Miller M, Simmons K, Weil KS. Mater Sci Eng C 2005;25:336–42.
[49] Deville S et al. Nat Mater 2009;8(12):966–72.
[50] Gibson LJ, Ashby, Michael F. Cellular solids: structure & properties. Cambridge University Press; 1999. p. 532.
[51] Wen CE et al. J Mater Sci – Mater Med 2002;13(4):397–401.
[52] Park C, Nutt SR. Mater Sci Eng A 2001;299(1–2):68–74.
[53] ASTM-F1580-07. Standard specification for titanium and titanium-6 aluminum-4 vanadium alloy powders for coatings of surgical implants.
[54] ASTM-F67-06. A standard specification for unalloyed titanium, for surgical implant applications.
[55] Li HL et al. Mater Trans 2004;45(4):1124–31.
[56] Imwinkelried T. J Biomed Mater Res A 2007;81A(4):964–70.
[57] Ide T et al. J Mater Res 2006;21(1):185–93.
[58] Ikeda T, Aoki T, Nakajima H. Metall Mater Trans A 2005;36A(1):77–86.
[59] Hyun SK, Murakami K, Nakajima H. Mater Sci Eng A 2001;299(1–2):241–8.
[60] Hyun SK, Nakajima H. Mater Sci Eng A 2003;340(1–2):258–64.
[61] Nakajima H. Prog Mater Sci 2007;52(7):1091–173.